# Cosmic star formation history revealed by *AKARI* and Hyper Suprime-Cam

Tomotsugu Goto,[1] Nagisa Oi,[2] Rieko Momose,[1] Ece Kilerci Eser,[1] Hideo Matsuhara,[3] Ting-Chi Huang,[1] Yousuke Utsumi,[4] Yoshiki Toba,[5] Youichi Ohyama,[5] Toshinobu Takagi,[6] Takehiko Wada,[3] Matthew Malkan,[7] Seong Jin Kim,[1] Takao Nakagawa,[3] and the *AKARI* team

[1] *National Tsing hua University, No. 101, Section 2, Kuang-Fu Road, Hsinchu, Taiwan 30013*

[2] *Tokyo University of Science, 1-3 Kagurazaka, Shinjuku-ku, Tokyo 162-8601, Japan*

[3] *Institute of Space and Astronautical Science, Japan Aerospace Exploration Agency, 3-1-1 Yoshinodai, Chuo, Sagamihara, Kanagawa 252-5210, Japan*

[4] *Kavli Institute for Particle Astrophysics and Cosmology (KIPAC), SLAC National Accelerator Laboratory, Stanford University, SLAC, 2575 Sand Hill Road, Menlo Park, CA 94025, USA*

[5] *Academia Sinica Institute of Astronomy and Astrophysics, P.O. Box 23-141, Taipei 10617, Taiwan*

[6] *Japan Space Forum, 3-2-1, Kandasurugadai, Chiyoda-ku, Tokyo 101-0062 Japan*

[7] *Department of Physics and Astronomy, UCLA, Los Angeles, CA, 90095-1547, USA*

## ABSTRACT

Understanding infrared (IR) luminosity is fundamental to understanding the cosmic star formation history and AGN evolution, since their most intense stages are often obscured by dust. Japanese infrared satellite, *AKARI*, provided unique data sets to probe this both at low and high redshift; the *AKARI* all sky survey in 6 bands (9–160 $\mu$m), and the *AKARI* NEP survey in 9 bands (2–24 $\mu$m). The *AKARI* performed all sky survey in 6 IR bands (9, 18, 65, 90, 140, and 160 $\mu$m) with 3–10 times better sensitivity than *IRAS*, covering the crucial far-IR wavelengths across the peak of the dust emission. Combined with a better spatial resolution, we measure the total infrared luminosity ($L_{\mathrm{TIR}}$) of individual galaxies, and thus, the total infrared luminosity density of the local Universe much more precisely than previous work.

In the *AKARI* NEP wide field, *AKARI* has obtained deep images in the mid-infrared (IR), covering 5.4 deg$^2$. However, our previous work was limited to the central area of 0.25 deg$^2$ due to the lack of deep optical coverage. To rectify the situation, we used the newly advent Subaru telescope's Hyper Suprime-Cam to obtain deep optical images over the entire 5.4 deg$^2$ of the *AKARI* NEP wide field. With this deep and wide optical data, we, for the first time, can use the entire *AKARI* NEP wide data to construct restframe 8um, 12um, and total infrared (TIR) luminosity functions (LFs) at $0.15 < z < 2.2$. A continuous 9-band filter coverage in the mid-IR wavelength (2.4, 3.2, 4.1, 7, 9, 11, 15, 18, and 24 $\mu$m by the *AKARI* satellite allowed us to estimate restframe 8 $\mu$m and 12 $\mu$m luminosities without using a large extrapolation based on a SED fit, which was the largest uncertainty in previous work.

By combining these two results, we reveal dust-hidden cosmic star formation history and AGN evolution from $z = 0$ to $z = 2.2$, all probed by the *AKARI* satellite.

## 1. LOCAL IR LF FROM *AKARI* ALL SKY SURVEY

Local infrared (IR) luminosity functions (LFs) are necessary benchmarks for high-redshift IR galaxy evolution studies. Any accurate IR LF evolution studies require accordingly accurate local IR LFs.

We construct infrared galaxy LFs at redshifts of $z \leq 0.3$ from *AKARI* space telescope, which performed an all-sky survey in six IR bands (9, 18, 65, 90, 140 and 160 $\mu$m) with 3–10 times better sensitivity than its precursor *IRAS*. Availability of 160 $\mu$m filter is critically important in accurately measuring total IR luminosity of galaxies, covering across the peak of the dust emission. By combining mid-IR data from Wide-field Infrared Survey Explorer (*WISE*), and spectroscpic redshifts from Sloan Digital Sky Survey (SDSS) Data Release 13 (DR13), 6-degree Field Galaxy Survey (6dFGS) and the 2MASS Redshift Survey (2MRS), we created a sample of 15,638 local IR galaxies with spectroscopic redshifts, by a factor of 20 larger compared with well-cited previous work based on *IRAS* data (Sanders et al. 2003a), which was also limited to <100 $\mu$m.

Corresponding author: Tomotsugu Goto
tomo@phys.nthu.edu.tw

T. GOTO ET AL.
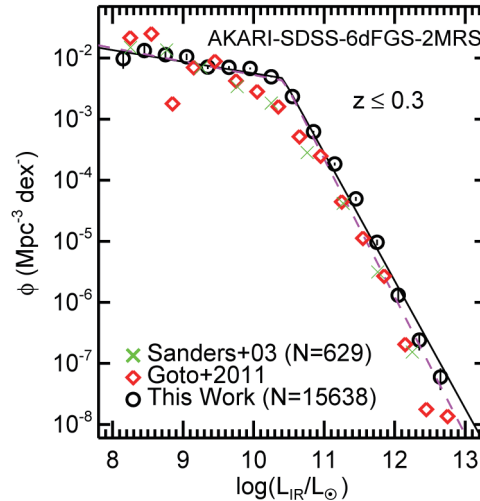


**Figure 1.** The IR LF of 15,638 *AKARI−SDSS−6dFGS−2MRS* galaxies (open circles). The best-fitting double power law is shown as solid line. For comparison the total IR LF derived from the *IRAS* RBGS is shown (crosses Sanders et al. 2003b). The red diamonds are the $1/V_{\mathrm{max}}$ data points of the RBGS sample adopted from Goto et al. (2011b). The dashed magenta line is the best-fitting double power law when the RBGS data are included in the fit.

After carefully correcting for volume effects in both IR and optical, we show obtained IR LFs in Figure 1, which agree well with previous studies, but comes with much smaller errors. Especially both faint- and bright-ends of the LFs are better-determined, due to much larger size of the spectroscpic redshifts and the IR photometry.

Measured local IR luminosity density is $\Omega_{\mathrm{IR}} = 1.19 \pm 0.05 \times 10^8 L_\odot$ Mpc$^{-3}$. The contributions from luminous infrared galaxies and ultra luminous infrared galaxies to $\Omega_{\mathrm{IR}}$ are very small, 9.3 per cent and 0.9 per cent, respectively. There exists no future all sky survey in far-infrared wavelengths in the foreseeable future. The IR LFs obtained in this work will therefore remain an important benchmark for high-redshift studies for decades. See more details in Kilerci Eser & Goto (2017).

## 2. HIGH-Z IR LFS FROM THE AKARI NEP WIDE FIELD

### 2.1. Undetected AKARI sources

The extragalactic background suggests at least half the energy generated by stars has been reprocessed into the infrared (IR) by dust (Lagache et al. 1999). At $z \sim 1.3$, 90% of star formation is obscured by dust (Le Floc'h et al. 2005; Goto et al. 2010b, 2015). Therefore, a full understanding of the cosmic star formation history inevitably needs an IR perspective, especially at high redshifts.

The *AKARI* space telescope has performed a deep mid-infrared imaging survey in the NEP region (Lee et al. 2009). We are studying the multi-band data of these mid-IR galaxies as shown in Table 1 (Takagi et al. 2010; Goto et al. 2010b). However, because very dusty objects cannot be detected in the relatively shallow CFHT imaging data ($r < 25.9$ ABmag; Oi et al. 2014), there remain 11,000 *AKARI* sources undetected in the optical. As a result, we lack understanding of the redshift and IR luminosity of these sources, i.e., they have been excluded from the past cosmic star formation history (CSFH) analysis. These sources could change our view of CSFH—if they all lie at $1 < z < 2$, they will *double* the cosmic star formation density at that epoch.

### 2.2. Uniqueness of *AKARI* mid-IR data

The *AKARI* NEP is one of the best fields for this investigation, due to the availability of continuous 9-band mid-IR filters. *Spitzer* lacks filters between 8 and 24 $\mu$m (the critical wide gap between IRAC and MIPS, excluding the tiny IRS peak up array at 16 $\mu$m). Similarly *WISE* also has a wide gap between 4 and 12 $\mu$m filters. Therefore, no other telescope can provide continuous 9-band photometry in mid-IR wavelength (2–24 $\mu$m) over 5.4 deg$^2$, until *JWST* performs a similar survey. *JWST* will also require a large amount of telescope time to survey 5.4 deg$^2$. *AKARI*'s continuous 9-band photometry works as a low-resolution spectrum, which is critically important for the following key aspects:

- Two physical processes produce the mid-IR emission: hot dust around an AGN, and PAH emission from star-formation. Quantitatively separating these is of fundamental importance. The continuous 9 filters of *AKARI* have made this possible through precise SED fitting (See examples in Takagi et al. 2010; Karouzos et al. 2014). Importantly, this is independent of extinction.

- Accurately measuring the mid-IR emission line strength (PAH 7.7 $\mu$m) and continuum luminosity. Using the 9-band photometry as a low-resolution spectra, Ohyama et al. (2017, submitted) demonstrated that photometric PAH 7.7 $\mu$m line measurements agree well with spectroscopic ones.
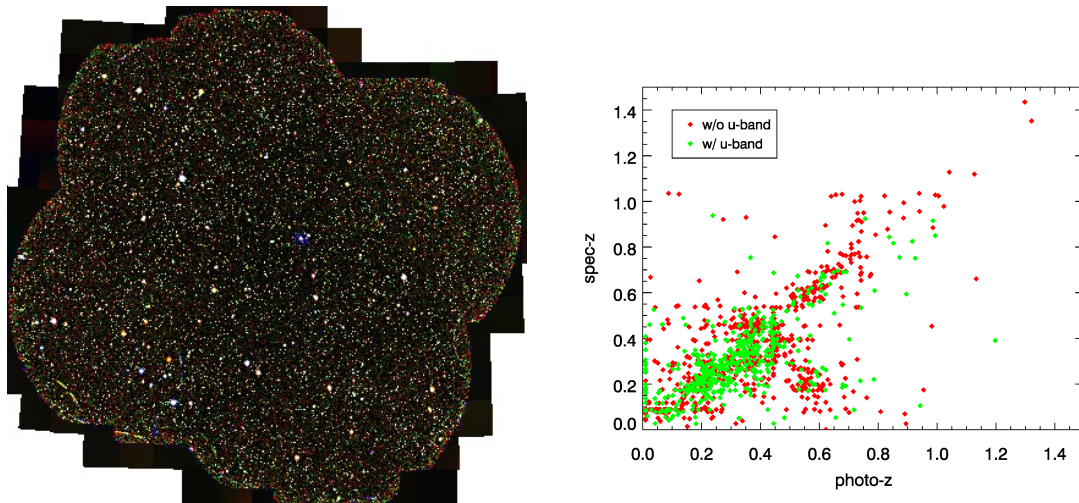
**Figure 2.** (left) HSC three color $(g, r, i)$ composite image of the NEP wide field (5.4 deg$^2$). For the first time, the entire NEP wide field was covered with deep optical data ($g \sim 27.2$).
(right) Photometric redshifts against spectroscopic redshifts. The sample with the CFHT $u^*$-band magnitude is plotted in green, while the sample without the CFHT $u^*$-band magnitude is plotted in red.

Neither of these is possible if there is a large gap between mid-IR filters. Therefore, *AKARI* NEP is the only field, where the two different astrophysical power sources can be separated for thousands of IR galaxies, including those with heavy extinction.

The *AKARI* NEP also has been thoroughly observed in every other available waveband (Table 1), making it one of the premier large deep fields on the sky. Its large area overcomes the serious problem of cosmic variance, which hampered previous IR CSFH studies. In particular, *Spitzer*'s CDFS field was only 0.25 deg$^2$ (Le Floc'h et al. 2005), and measured an IR luminosity density nearly a factor of 10 different from other *Spitzer* fields (e.g., Babbedge et al. 2006). For the same reason, the single Suprime-Cam pointing in the center of the NEP deep field (0.25 deg$^2$) is not wide enough. A large volume coverage also allows us to study environmental effects on galaxy evolution (Koyama et al. 2008; Goto et al. 2010a). *AKARI* was a survey telescope, which observed 5.4 deg$^2$ in NEP using ~10% of the entire pointed observations available throughout the lifetime of the mission, providing uniquely precious space-based IR data spanning a large enough area to overcome cosmic variance.

## 2.3. **Subaru Hyper Suprime-Cam Observation**

However, previously, we only had deep optical images in the central 0.25 deg$^2$, while previous *AKARI*'s mid-IR data exist in much larger field of 5.4 deg$^2$. Therefore, our previous work also suffered from the cosmic variance.

To rectify the situation, we carried out an optical survey of the *AKARI* NEP wide field using Subaru's new Hyper Suprime-Cam (HSC; Miyazaki et al. 2012). The HSC has a field-of-view (FoV) of 1.5 deg in diameter, covered with 104 red-sensitive CCDs. It has the largest FoV among optical cameras on an 8m telescope, and can cover the *AKARI* NEP wide field (5.4 deg$^2$) with only 4 FoV (the left panel of Figure 2).

Our immediate aim of the optical survey is to detect all *AKARI* sources in the optical, with photometry accurate enough for reliable photometric redshifts. This allows us to determine the optical and IR luminosities (corresponding to direct and dust-obscured emission) from young stars and accreting massive black holes for a large sample representative of the cosmic history of the Universe.

Our proposal to the Subaru telescope was accepted twice (PI: T.Goto). In 2014, we were limited to the $r$-band observation due to unexpected unavailability of the filter stacker of HSC caused by the instrument troubles propagated from the telescope chiller trouble. We observed in $r$ in 7 FoVs with sets of 5 point dithering pattern with the seeing of $\sim 1\farcs 5$.

In 2016, we obtained data in the remaining $g, i, z, y$ filters in 4 FoV covering the NEP wide field. The 5 sigma limiting magnitudes are 27.18, 26.71, 26.10, 25.26, and 24.78 mag [AB] in $g, r, i, z$, and $y$-bands, respectively. See Oi et al. in this volume for more details of the observation and data reduction.

## 2.4. **CFHT $u^*$-band observation**

Subaru telescope does not have a $u^*$-band imaging capability, while it is critically important to accurately estimate photometric redshifts of low-$z$ galaxies. Therefore, we obtained $u^*$-band image of the *AKARI* NEP wide field using the Megaprime camera of Canada France Hawaii Telescope (CFHT, PI: T.Goto). See more details of the observation and data reduction in Appendix.

T. Goto et al.

**Table 1.** Summary of *AKARI* NEP survey data

| Observatory | Band | Sensitivity/Number of objects/exposure time | Area (deg$^2$) |
|---|---|---|---|
| ***AKARI*/IRC** | **2.5–24 $\mu$m** | $L15 = 18.5$AB | **5.4** |
| Subaru/S-Cam | $BVRi'z'$ | $R = 27.4$AB | 0.25 |
| Subaru/FOCAS | optical spec. | 57 sources in NEP, $R \sim 24$AB | 0.25 |
| MMT6m | optical spec. | $\sim$1800 obj | 5.4 |
| KPNO-2.1m | $J, H$ | 21.6, 21.3 | 5.4 |
| Maidanak 1.5m | $B, R, I$ | $R = 23.1$ | 3.4 |
| KPNO2m/FLAMINGOS | $J, H$ | $J = 21.6, H = 21.3$ | 5.4 |
| WIRCAM | Y, J, K | 24AB | 1 |
| *GALEX* | NUV, FUV | NUV=26 | 1.5 |
| WSRT | 20 cm | $\sim$100 $\mu$Jy | 0.25 |
| VLA-archive | 10 cm | 200 $\mu$Jy | 5.4 |
| GMRT | 610 MHz | 60–80 $\mu$Jy | 0.25 |
| Keck/Deimos | optical spec. | $\sim$1000 obj | 0.25 |
| Subaru/FMOS | near-IR spec. | $\sim$700 obj | 0.25 |
| *Herschel* | 100, 160 $\mu$m | 5–10 mJy | 0.5 |
| *Herschel* | 250–500 $\mu$m | $\sim$10 mJy | 7.1 |
| *Chandra* | X-ray | 30–80 ks | 0.25 |
| SCUBA2 | submm | 1 mJy | 0.25 |
| **CFHT/MegaCam** | $u^*griz$ | $r \leq 25.9$AB | **4** |
| **Subaru/HSC** | $g, r, i, z, y$ | $r = 27.2$ (Figure 2) | **5.4** |

## 2.5. Photometric redshift

Using CFHT $u^*$-band, and HSC $g, r, i, z, y$-bands data, we calculated photometric redshifts with the LePhare code (Arnouts et al. 2007). We used the COSMOS galaxy library for SED fitting (Ilbert et al. 2009). Extinction law from Calzetti et al. (2005) was applied in the SED fitting. Also, we adopted the function AUTO_ADAPT in LePhare to adjust magnitude zero points. In the SED fitting, we used 29 bands in maximum from the following instruments, *GALEX* ($FUV, NUV$), CFHT ($u^*$), HSC ($g, r, i, z, y$), *AKARI* ($N2, N3, N4, S7, S9, S11, L15, L18, L24$), *WISE* ([3.4], [4.6], [12], [22]), *Spitzer* ([3.6], [4.5], [5.8], [8.0], [24]), Herschel ($PSW, PMW, PLW$). Note not all data are available for all the *AKARI* sources.

By comparing with spectroscopic redshifts, we examine the accuracy of photo-$z$. The $\sigma$ is defined to be the standard deviation of $\frac{\triangle z}{1 + z_s}$ for $\frac{\triangle z}{1 + z_s} < 0.15$, where the $\triangle z$ is $|z_p - z_s|$ and $z_p$ and $z_s$ are the photometric and spectroscopic redshifts, respectively. The fraction of the objects with $\frac{\triangle z}{1 + z_s} > 0.15$ is defined to be the catastrophic rate $\eta$. The main result is shown in the right panel of Figure 2. The ($\sigma$, $\eta$) are (0.038, 17.6%), (0.039, 21.6%), and (0.036, 12.4%) for the whole sample, the sample without $u^*$-band (red), and the sample with $u^*$-band, respectively. The $u^*$-band data improve both $\sigma$ and $\eta$.

## 2.6. Analysis

We compute LFs using the $1/V_{max}$ method, as in Goto et al. (2010b, 2015). Uncertainties of the LF values stem from various factors such as fluctuations in the number of sources in each luminosity bin, the photometric redshift uncertainties, the $k$-correction uncertainties, and the flux errors. To compute the errors of LFs we performed Monte Carlo simulations by creating 1000 simulated catalogs. Each simulated catalog contains the same number of sources, but we assigned a new redshift to each source, by following a Gaussian distribution centered at the photometric redshift with the measured dispersion $\Delta z/(1 + z)$. The flux of each source is also changed; the new fluxes vary according to the measured flux error following a Gaussian distribution.

For the 8 $\mu$m and the 12 $\mu$m LFs, we can ignore the errors due to the $k$-correction thanks to the continuous *AKARI* MIR filter coverage. The TIR LF errors are estimated by re-performing the SED fitting for each of the 1000 simulated catalogs.

We did not consider the uncertainty related to cosmic variance here since our field coverage has been significantly improved. For our analysis, each redshift bin covers $\sim 2 \times 10^7$ Mpc$^3$ of volume, which is large enough to avoid significant effect from the cosmic variance. See Matsuhara et al. (2006) for more discussion on the cosmic variance in the NEP field.

All the other errors described above are added to the Poisson errors for each LF bin in quadrature.

## 2.7. Results: High-z IR LFs

### 2.7.1. The 8 $\mu$m LF

Monochromatic 8 $\mu$m luminosity ($L_{8\mu m}$) is known to correlate well with the TIR luminosity (Babbedge et al. 2006; Huang et al. 2007; Goto et al. 2011a), especially for star-forming galaxies, because the rest-frame 8 $\mu$m flux is dominated by prominent PAH (polycyclic aromatic hydrocarbon) features such as those at 6.2, 7.7, and 8.6 $\mu$m.

Since *AKARI* has continuous coverage in the mid-IR wavelength range, the restframe 8 $\mu$m luminosity can be obtained without a large uncertainty in $k$-correction at the corresponding redshift and filter. For example, at $z = 0.375$, restframe 8 $\mu$m is redshifted into $S11$ filter. Similarly, $L15$, $L18W$ and $L24$ cover restframe 8 $\mu$m at $z = 0.775$, 1.25 and 2. This filter
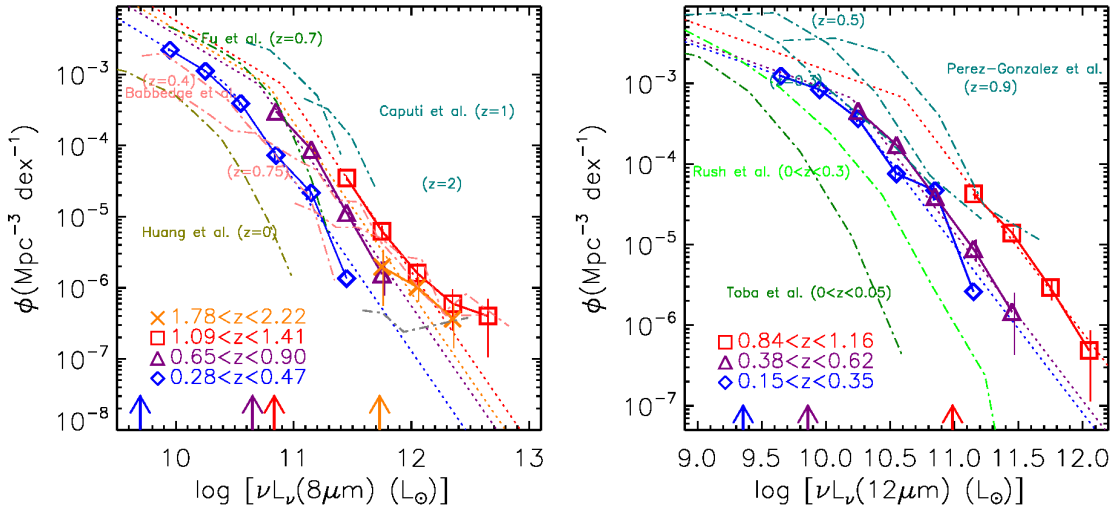
**Figure 3.** (left) Restframe 8 $\mu$m LFs based on the *AKARI* NEP wide field. The blue diamonds, the purple triangles, the red squares, and the orange crosses show the 8 $\mu$m LFs at $0.28 < z < 0.47$, $0.65 < z < 0.90$, $1.09 < z < 1.41$, and $1.78 < z < 2.22$, respectively. *AKARI*'s MIR filters can observe restframe 8 $\mu$m at these redshifts in a corresponding filter. Error bars are estimated from the Monte Caro simulations (§2.6). The dotted lines show analytical fits with a double-power law. Vertical arrows show the 8 $\mu$m luminosity corresponding to the flux limit at the central redshift in each redshift bin. Overplotted are Babbedge et al. (2006) in the pink dash-dotted lines, Caputi et al. (2007) in the cyan dash-dotted lines, Huang et al. (2007) in the dark-yellow dash-dotted lines, and Fu et al. (2010) in the green dash-dotted line.

(right) Restframe 12 $\mu$m LFs based on the *AKARI* NEP wide field. Luminosity unit is logarithmic solar luminosity ($L_\odot$). The blue diamonds, the purple triangles, and the red squares show the 12 $\mu$m LFs at $0.15 < z < 0.35$, $0.38 < z < 0.62$, and $0.84 < z < 1.16$, respectively. Vertical arrows show the 12 $\mu$m luminosity corresponding to the flux limit at the central redshift in each redshift bin. Overplotted are Pérez-González et al. (2005) at $z = 0.3$, 0.5 and 0.9 in the dark-cyan dash-dotted lines, Toba et al. (2014) at $0 < z < 0.05$ based on *WISE* in the dark green dash-dotted lines, and Rush et al. (1993) at $0 < z < 0.3$ in the light green dash-dotted lines. Note Rush et al. (1993) is at higher redshifts than Toba et al. (2014).

coverage is an advantage with *AKARI* data. Often in previous work, SED models were used to extrapolate from *Spitzer* 24 $\mu$m fluxes, producing the largest uncertainty. This is not the case for the analysis present in this paper.

To obtain the restframe 8 $\mu$m LF, we used sources down to 80% completeness limits in each band as measured in Kim et al. (2012). We excluded those galaxies whose SEDs are better fit with QSO templates. This removed 2% of galaxies from the sample.

We used the completeness curve presented in Kim et al. (2012) to correct for the incompleteness of the detections. However, this correction is 25% at maximum, since our sample is brighter than the 80% completeness limits. Our main conclusions are not affected by this incompleteness correction. To compensate for the increasing uncertainty at increasing $z$, we use four redshift bins of $0.28 < z < 0.47$, $0.65 < z < 0.90$, $1.09 < z < 1.41$, and $1.78 < z < 2.22$. Within each redshift bin, we use the $1/V_{max}$ method to compensate for the flux limit in each filter.

We show the computed restframe 8 $\mu$m LF in the left panel of Figure 3. The arrows mark the 8 $\mu$m luminosity corresponding to the flux limit at the central redshift in each redshift bin. Errorbars on each point are based on the Monte Carlo simulation, and are smaller than in our previous work (Goto et al. 2010b). To compare with previous work, the dark-yellow dot-dashed line also shows the 8 $\mu$m LF of star-forming galaxies at $0 < z < 0.3$ by Huang et al. (2007), using the $1/V_{max}$ method applied to the IRAC 8 $\mu$m GTO data. Compared to the local LF, our 8 $\mu$m LFs show strong evolution in luminosity.

## 2.8. **12 $\mu$m LF**

The 12 $\mu$m luminosity ($L_{12\mu m}$) has been well studied through *ISO* and *IRAS*. It is known to correlate closely with the TIR luminosity (Spinoglio et al. 1995; Pérez-González et al. 2005). As was the case for the 8 $\mu$m LF, it is advantageous that *AKARI*'s continuous filters in the mid-IR allow us to estimate restframe 12 $\mu$m luminosity without much extrapolation based on SED models.

At targeted redshifts of $z = 0.25$, 0.5, and 1, the $L15$, $L18W$ and $L24$ filters cover the restframe 12 $\mu$m, respectively. The methodology is the same as for the 8 $\mu$m LF; we used the sample down to the 80% completeness limit, corrected for the incompleteness, then used the $1/V_{max}$ method to compute the LF in each redshift bin. The resulting 12 $\mu$m LF is shown in the right panel of Figure 3. The light green dash-dotted line shows 12 $\mu$m LF based on 893 galaxies at $0 < z < 0.3$ in the *IRAS* Faint Source Catalog (Rush et al. 1993). The dark green dash-dotted line shows 12 $\mu$m LF at $0.006 < z < 0.05$
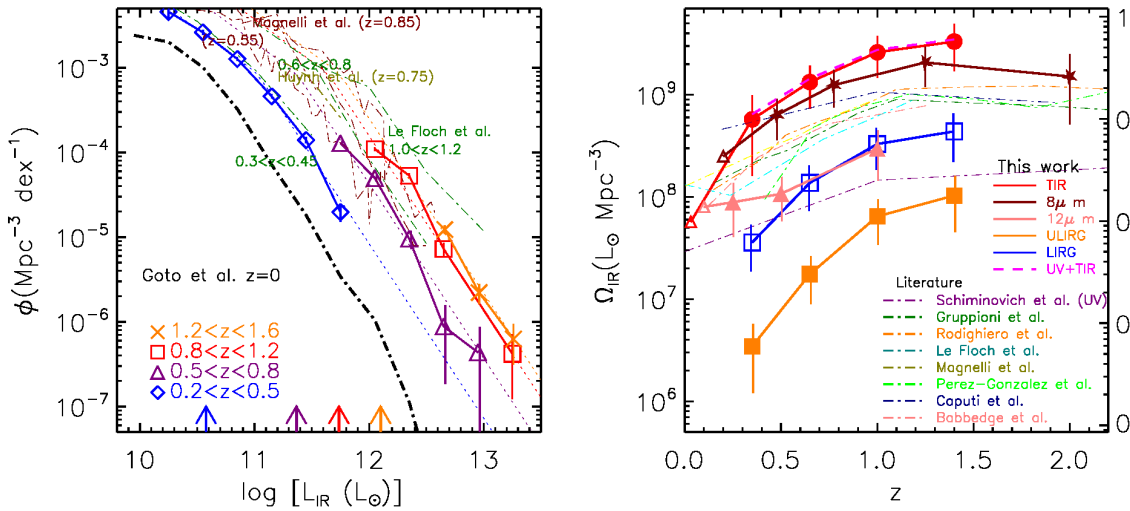
**Figure 4.** (left) The TIR LFs from the SED fit. Vertical arrows show the luminosity corresponding to the flux limit at the central redshift in each redshift bin. We overplot z=0 IR LF based on the *AKARI* FIR all sky survey in the black dash-dot line (Goto et al. 2011a; Kilerci Eser & Goto 2017). Overplotted previous studies are taken from Le Floc'h et al. (2005) in the dark-green, dash-dotted line, Magnelli et al. (2009) in the dark-red, dash-dotted line, and Huynh et al. (2007) in the dark-yellow, dash-dotted line at several redshifts as marked in the figure.

(right) The evolution of the TIR luminosity density based on TIR LFs (red circles), 8 $\mu$m LFs (stars), and 12 $\mu$m LFs (filled triangles). The blue open squares and orange filled squares are for LIRG and ULIRGs only, also based on our $L_{TIR}$ LFs. Overplotted dot-dashed lines are estimates from the literature: Le Floc'h et al. (2005), Magnelli et al. (2009), Pérez-González et al. (2005), Caputi et al. (2007), Gruppioni et al. (2013), Rodighiero et al. (2010), and Babbedge et al. (2006) are in cyan, yellow, green, navy, dark green, orange, and pink, respectively. The purple dash-dotted line shows the UV estimate by Schiminovich et al. (2005). The pink dashed line shows the total estimate of IR (TIR LF) and UV (Schiminovich et al. 2005). The open triangles are low-z results from Goto et al. (2011a); Huang et al. (2007); Toba et al. (2014) in TIR, 8 $\mu$m and 12 $\mu$m, respectively.

based on 223,982 galaxies from *WISE* sources in Table 7 of Toba et al. (2014). Compared with these $z = 0$ LFs, the 12 $\mu$m LFs show steady evolution with increasing redshift.

## 2.9. Total IR LFs

*AKARI*'s continuous mid-IR coverage is also superior for SED-fitting to estimate $L_{\rm TIR}$. This is because for star-forming galaxies, the mid-IR part of the IR SED is dominated by the PAH emission lines, which reflect the SFR of galaxies (Genzel et al. 1998), and thus, correlates well with $L_{\rm TIR}$, which is also a good indicator of the galaxy SFR.

After photometric redshifts are estimated using the UV-optical-NIR photometry, we fix the redshift at the photo-$z$, then use the same LePhare code to fit the infrared part of the SED to estimate TIR luminosity. We used Lagache et al. (2003)'s SED templates to fit the photometry using the *AKARI* bands at $> 6$ $\mu$m ($S7$, $S9W$, $S11$, $L15$, $L18W$ and $L24$).

In the mid-IR, color-correction could be large when strong PAH emissions shift into the bandpass (a factor of ~3). However, during the SED fitting, we integrate the flux over the bandpass weighted by the response function. Therefore, we do not use the flux at a fixed wavelength. As such, the color-correction is negligible in our process (a few percent at most).

Galaxies in the targeted redshift range are best sampled in the 18 $\mu$m band due to the wide bandpass of the $L18W$ filter (Matsuhara et al. 2006). Therefore, we applied the $1/V_{\rm max}$ method using the detection limit at $L18W$. We also checked that using the $L15$ flux limit does not change our main results. The same Lagache et al. (2003)'s models are also used for $k$-corrections necessary to compute $V_{\rm max}$ and $V_{\rm min}$. The redshift bins used are $0.2 < z < 0.5$, $0.5 < z < 0.8$, $0.8 < z < 1.2$, and $1.2 < z < 1.6$.

The obtained $L_{\rm TIR}$ LFs are shown in the left panel of Figure 4. The uncertainties are estimated through the Monte Carlo simulations (§2.6). For a local benchmark, we overplot Kilerci Eser & Goto (2017) from the *AKARI* all sky survey in § 1. The TIR LFs show a strong evolution compared to local LFs.

## 2.10. Total IR Luminosity density

One of the important purposes in computing IR LFs is to estimate the IR luminosity density, which in turn is an extinction-free estimator of the cosmic star formation density (Kennicutt 1998). We estimate the total infrared luminosity density by integrating the LF weighted by the luminosity. First, we need to convert $L_{8\mu m}$ to the total infrared luminosity.

A strong correlation between $L_{8\mu m}$ and total infrared luminosity ($L_{\rm TIR}$) has been reported in the literature (Caputi et al. 2007; Bavouzet et al. 2008). Using a large sample of 605 galaxies detected in the far-infrared by the *AKARI* all sky survey,

**Table 2.** The configuration of extraction and photomety used for generating the CFHT $u^*$-band catalogue

| Parameter | Value |
|---|---|
| DETECT_TYPE | CCD |
| DETECT_MINAREA | 5 |
| DETECT_MINAREA | 0 |
| THRESH_TYPE | RELATIVE |
| DETECT_THRESH | 1.5 |
| ANALYSIS_THRESH | 5 |
| FILTER | Y |
| FILTER_NAME | gauss_3.0_7x7.conv |
| FILTER_THRESH | 1.0 |
| DEBLEND_NTHRESH | 32 |
| DEBLEND_MINCONT | 0.001 |
| CLEAN | Y |
| CLEAN_PARAM | 1.0 |
| MASK_TYPE | CORRECT |
| PHOT_APERTURES | 5 |
| PHOT_AUTOPARAMS | 2.5, 3.5 |
| PHOT_PETROPARAMS | 2.0, 3.5 |
| PHOT_AUTOAPERS | 0.0,0.0 |
| PHOT_FLUXFRAC | 0.5 |
| SATUR_LEVEL | 50000 |
| SATUR_KEY | SATURATE |
| MAG_ZEROPOINT | 25.26 |
| MAG_GAMMA | 4.0 |
| GAIN | 0.0 |
| GAIN_KEY | GAIN |
| PIXEL_SCALE | 1.0 |

Goto et al. (2011c) estimated the best-fit relation between $L_{8\mu m}$ and $L_{\rm TIR}$ as

$$L_{\rm TIR} = (20 \pm 5) \times \nu L_{\nu,8\mu m}^{0.94\pm0.01}(\pm44\%). \tag{1}$$

The $L_{\rm TIR}$ is based on *AKARI*'s far-IR photometry in 65, 90, 140, and 160 $\mu$m, and the $L_{8\mu m}$ measurement is based on *AKARI*'s 9 $\mu$m photometry. Given the superior statistics and availability over longer wavelengths (140 and 160 $\mu$m), we used this equation to convert $L_{8\mu m}$ into $L_{\rm TIR}$.

The 12 $\mu$m is one of the most frequently used monochromatic fluxes to estimate $L_{\rm TIR}$. The total infrared luminosity can be computed from the $L_{12\mu m}$ using the conversion in Chary & Elbaz (2001); Pérez-González et al. (2005).

$$\log L_{\rm TIR} = \log(0.89^{+0.38}_{-0.27}) + 1.094 \log L_{12\mu m} \tag{2}$$

The 8, 12 $\mu$m and total LFs are weighted by the $L_{\rm TIR}$ and integrated to obtain the TIR density. For integration, we first fitted an analytical function to the LFs.

In this work, a double-power law is fitted to the lowest redshift LF to determine the normalization ($\Phi^*$) and slopes ($\alpha, \beta$). For higher redshifts we do not have enough statistics to simultaneously fit 4 parameters ($\Phi^*$, $L^*$, $\alpha$, and $\beta$). Therefore, we fixed the slopes and normalization at the local values and varied only $L^*$ for the higher-redshift LFs. Fixing the faint-end slope is a common procedure with the depth of current IR satellite surveys (Babbedge et al. 2006; Caputi et al. 2007). The stronger evolution in luminosity than in density found by previous work (Pérez-González et al. 2005; Le Floc'h et al. 2005) also justifies this parametrization.

The best-fit power-laws are shown with dotted-lines in Figures 3 and 4. Once the best-fit parameters are found, we integrate the double power law outside the luminosity range in which we have data to estimate the TIR luminosity density, $\Omega_{\rm TIR}$. In the right panel of Figure 4, we plot $\Omega_{\rm IR}$ estimated from the TIR LFs (red circles), 8 $\mu$m LFs (brown stars), and 12 $\mu$m LFs (pink filled triangles). All our measurements show a strong evolution as a function of redshift.

We also plot the contributions to $\Omega_{\rm IR}$ from LIRGs (Luminous InfraRed Galaxies; $L_{\rm TIR} > 10^{11} L_\odot$) and ULIRGs (Ultra-Luminous InfraRed Galaxies; $L_{\rm TIR} > 10^{12} L_\odot$, measured from TIR LFs), with the blue open squares and orange filled squares, respectively. Both LIRGs and ULIRGs show a strong redshift evolution.

## ACKNOWLEDGMENTS

## APPENDIX

### A. **APPENDIX: CFHT $U^*$-BAND OBSERVATION AND DATA REDUCTION**

Here we summarize our CFHT $u^*$-band observation and data reduction. The purpose of the $u^*$-band observation is to provide a $u^*$-band catalogue in *AKARI* NEP wide field and then estimate accurate photometric redshifts with the aid of the $u^*$-band magnitude. The Megaprime $u^*$-band ranges from 3235 Å to 4292 Å with the effective wavelength at 3827.2 Å. The observations were carried out in two time periods from 2015 May 22nd to 26th, and from 2016 July 6th to 7th (PI: T.Goto). There are 66 frames in total, which cover the 4.5 deg$^2$ of *AKARI* NEP field. The exposure time is 300 second for each frame. Megaprime has 40 CCDs with 2048 × 4612 pixels for each. The pixel scale is 0.185 arcsec per pixel.

T. GOTO ET AL.

We used the Elixir pipeline to reduce our raw $u^*$-band data. We masked bad pixels, bias structures and corrected for flat-fields. The pipeline had some problem with removing overscan regions, so we manually wrote a script to remove them. The zero point magnitude measured for camera runs are 25.188 and 25.121.

To create a coadded image, we utilized AstrOmatic softwares including SExtractor, SCAMP and SWarp. First, we used SExtractor to extract sources and performed photometry. Second, SCAMP help us with astrometric calibration. In this process, we used 2MASS $J$-band observation as a reference catalogue for astrometry. Third, we coadd images from each frames by SWarp. Each pixel value is the median of every combined pixels. We include background subtraction with mesh size of 128 pixels. Last but not least, we ran SExtractor again on the final coadded image to obtain the $u^*$-band catalogue. The configuration of extraction and photometry is listed in Table 2. We cross-matched the $u^*$-band catalogue with the Subaru HSC catalogue in the *AKARI* NEP field by matching celestial coordinate within 1 arcsec tolerance radius.

The magnitude is calculated by the following equation.

$$m = -2.5 \times \log(\text{data number}) + 2.5 \times \log(\text{exposure time}) + m_0 + K \times (\text{airmass} - 1)$$

The $m_0$ is the zero point magnitude with value 25.121. The $K$ is a coefficient for airmass term correction, of which value is $-0.35$. Finally, we calibrated the $u^*$-band magnitude with the $u^*$-band of the *AKARI* NEP deep field, which is a 0.6 deg$^2$ sub-region of the *AKARI* NEP field (Oi et al. 2014).

## REFERENCES

Arnouts, S., Walcher, C. J., Le Fèvre, O., et al. 2007, A&A, 476, 137

Babbedge, T. S. R., Rowan-Robinson, M., Vaccari, M., et al. 2006, MNRAS, 370, 1159

Bavouzet, N., Dole, H., Le Floc'h, E., et al. 2008, A&A, 479, 83

Calzetti, D., Kennicutt, Jr., R. C., Bianchi, L., et al. 2005, ApJ, 633, 871

Caputi, K. I., Lagache, G., Yan, L., et al. 2007, ApJ, 660, 97

Chary, R. & Elbaz, D. 2001, ApJ, 556, 562

Fu, H., Yan, L., Scoville, N. Z., et al. 2010, ApJ, 722, 653

Genzel, R., Lutz, D., Sturm, E., et al. 1998, ApJ, 498, 579

Goto, T., Arnouts, S. Malkan, M., et al. 2011a, MNRAS, 414, 1903

Goto, T., Arnouts, S., Inami, H., et al. 2011b, MNRAS, 410, 573

Goto, T., Arnouts, S., Inami, H., et al. 2011c, MNRAS, 410, 573

Goto, T., Koyama, Y., Wada, T., et al. 2010a, A&A, 514, A7

Goto, T., Oi, N., Ohyama, Y., et al. 2015, MNRAS, 452, 1684

Goto, T., Takagi, T., Matsuhara, H., et al. 2010b, A&A, 514, A6

Gruppioni, C., Pozzi, F., Rodighiero, G., et al. 2013, MNRAS, 432, 23

Huang, J.-S., Ashby, M. L. N., Barmby, P., et al. 2007, ApJ, 664, 840

Huynh, M. T., Frayer, D. T., Mobasher, B., et al. 2007, ApJL, 667, L9

Ilbert, O., Capak, P., Salvato, M., et al. 2009, ApJ, 690, 1236

Karouzos, M., Im, M., Trichas, M., et al. 2014, ApJ, 784, 137

Kennicutt, Jr., R. C. 1998, ARA&A, 36, 189

Kilerci Eser, E. & Goto, T. 2017, accepted, MNRAS[0903.4693]

Kim, S. J., Lee, H. M., Matsuhara, H., et al. 2012, A&A, 548, A29

Koyama, Y., Kodama, T., Shimasaku, K., et al. 2008, MNRAS, 391, 1758

Lagache, G., Abergel, A., Boulanger, F., Désert, F. X., & Puget, J.-L. 1999, A&A, 344, 322

Lagache, G., Dole, H., & Puget, J.-L. 2003, MNRAS, 338, 555

Le Floc'h, E., Papovich, C., Dole, H., et al. 2005, ApJ, 632, 169

Lee, H. M., Kim, S. J., Im, M., et al. 2009, PASJ, 61, 375

Magnelli, B., Elbaz, D., Chary, R. R., et al. 2009, A&A, 496, 57

Matsuhara, H., Wada, T., Matsuura, S., et al. 2006, PASJ, 58, 673

Miyazaki, S., Komiyama, Y., Nakaya, H., et al. 2012, in Proc. SPIE, Vol. 8446, , 84460Z

Oi, N., Matsuhara, H., Murata, K., et al. 2014, A&A, 566, A60

Pérez-González, P. G., Rieke, G. H., Egami, E., et al. 2005, ApJ, 630, 82

Rodighiero, G., Vaccari, M., Franceschini, A., et al. 2010, A&A, 515, A8

Rush, B., Malkan, M. A., & Spinoglio, L. 1993, ApJS, 89, 1

Sanders, D. B., Mazzarella, J. M., Kim, D.-C., Surace, J. A., & Soifer, B. T. 2003a, AJ, 126, 1607

Sanders, D. B., Mazzarella, J. M., Kim, D.-C., Surace, J. A., & Soifer, B. T. 2003b, AJ, 126, 1607

Schiminovich, D., Ilbert, O., Arnouts, S., et al. 2005, ApJL, 619, L47

Spinoglio, L., Malkan, M. A., Rush, B., Carrasco, L., & Recillas-Cruz, E. 1995, ApJ, 453, 616

Takagi, T., Ohyama, Y., Goto, T., et al. 2010, A&A, 514, A5

Toba, Y., Oyabu, S., Matsuhara, H., et al. 2014, ApJ, 788, 45